PHYSICAL REVIEW B **110**, 085111 (2024)

Electrical conductivity of goldene

Shuo Zhao, Huiwen Zhang, Mingfeng Zhu, Liwei Jiang, and Yisong Zheng[*]
Key Laboratory of Physics and Technology for Advanced Batteries (Ministry of Education)
and Department of Physics, Jilin University, Changchun 130012, China

(Received 6 June 2024; revised 20 July 2024; accepted 24 July 2024; published 6 August 2024)

As a noble metal, gold is known to possess ultrahigh conductivity and is therefore widely used as a conductor in a variety of integrated circuits. Recently, a two-dimensional (2D) material made of a single atomic layer of gold has been successfully produced, called goldene, after the name of graphene. This immediately raises an interesting question of whether goldene is an excellent conductor, comparable to its three-dimensional counterpart. In the present paper, by performing the first principles calculations on the conductivity of goldene arising from electron-phonon (eph) scattering, we find that such a 2D gold has a very high intrinsic conductivity at room temperature, which is in the same order of magnitudes as that of a lightly doped graphene and much larger than other 2D materials accessible so far. This result suggests that goldene, instead of its 3D bulk, is an excellent conductor in future electronic devices based on 2D materials, Then, we make a detailed analysis of the individual roles of the electronic structure and e-ph scattering strength in contributing to the intrinsic electric and thermal conductivity of goldene. Finally, we establish a simple deformational potential model to describe the e-ph interaction, which works very well to reproduce the numerical result of first-principles calculation of the intrinsic conductivity of goldene.

DOI: 10.1103/PhysRevB.110.085111

I. INTRODUCTION

It is well known that noble metals such as gold (Au) and silver (Ag) are widely used in a variety of electronic devices, such as chemical sensors [1], wires [2], and supercapacitors [3], owing to their excellent electronic transport property. Even in increasingly miniaturized computer chips, noble metals such as gold are still indispensable as wires for carrying current [4,5]. Of course, in these devices, the size of the gold conductor decreases with the whole device, eventually reaching the nanoscale [6,7]. In this context, the quantum confinement effect, lattice instability, and weak localization in mesoscopic regime becomes strong enough to affect the electronic transport property of gold wires. Therefore, whether the gold conductor at the nanoscale can still maintain excellent electrical conductivity becomes one of the key issues limiting the functionality of the devices.

Over the past two decades, starting with the successful fabrication of graphene, research into 2D materials has experienced rapid development, which provides us an unprecedented material platform for designing ultrathin electronic devices [8–10]. Some promising device prototypes such as field effect transistors and magnetic tunneling junctions are experimentally implemented or theoretically proposed based on a variety of 2D semiconductors and magnetic materials [11–16]. However, a 2D metallic material with high conductivity is always desirable for high performance and low-power device functionality. So far, graphene is believed to be the 2D materials with highest conductivity, but carrier doping is required [17]. Other metallic materials, such as MXenes [18,19] and MBenes [20,21], accessible so far have conductivities smaller than that of graphene by one or two orders of magnitudes. Therefore, an excellent 2D metallic material is still lacking to act as the wires in future devices, like gold in today's integrated circuits.

Given the excellent conductivity of 3D bulk materials of noble metals such as gold, it is natural to produce noble metal films with increasingly thinner thicknesses to be used as good 2D conductors. However, it remains a great challenge to fabricate a noble metal film with a thickness of single or a few atomic layers [6,7]. Until recently, a substantial breakthrough for the successful creation of single-atom-thick gold layers was realized by Kashiwaya *et al.* through wet chemical etching of Ti_3C_2 from nanolamellar Ti_3AuC_2. Such a 2D gold is dubbed as "goldene" because of its similar lattice structure with graphene [22]. This breakthrough immediately raises the interesting question of whether goldene is an excellent conductor, possessing high conductivity comparable to its three-dimensional counterpart. To answer this question, experimental measurements on goldene samples of macroscopic scale should be conducted. Meanwhile, a theoretical investigation of the electronic transport properties on this 2D gold material is also significant.

In the present paper, by performing the first-principles calculations we theoretically study the conductivity of goldene arising from electron-phonon (e-ph) scattering. It is known the e-ph interaction is inevitable even in a perfect lattice; hence, the e-ph scattering-limited conductivity is called the intrinsic conductivity, which dominantly determines the electronic transport property of most materials at and beyond room

---

[*] Contact author: zhengys@jlu.edu.cn

temperature. From numerical results, we find that goldene indeed has a high intrinsic conductivity at room temperature, which is of the same order of magnitudes as that of lightly doped graphene and significantly larger than other 2D materials available so far, such as the typical 2D materials in the families of MXenes and MBenes. In addition, the thermal conductivity of goldene is also found to be very large. These results suggest that goldene, like its 3D bulk, is an excellent conductor in future electronic devices based on 2D materials. Besides the first-principles calculations, we establish a simple acoustic deformational potential (ADP) model [23] to describe the e-ph interaction in goldene, which works very well to reproduce the numerical result of first principles calculation of the intrinsic conductivity and thermal conductivity of goldene.

The rest of this paper is organized as follows: In Sec. II, we provide a brief description of the theoretical approach, mainly consisting of the formulas about the Boltzmann transport equation to calculate the electronic transport properties. It is followed by Sec. III in which the technical details of the first-principles calculations is introduced. Then, the numerical results for the intrinsic conductivity of goldene are presented and discussed in Sec. IV. Finally, the main results are summarized in Sec. V.

II. BOLTZMANN EQUATION

In this paper we employ the semiclassical Boltzmann transport equation (BTE) to calculate the conductivity and thermal conductivity of goldene subject to the e-ph scattering. It is well known that the BTE for a macroscopically uniform system is established on the following equation [24,25]:

$$\left(\frac{\partial f_{n\boldsymbol{k}}}{\partial t}\right)_{\text{coll}} = -\left(\frac{\partial f_{n\boldsymbol{k}}}{\partial t}\right)_{\text{diff}}, \tag{1}$$

which says that the variations of electronic distribution function ($f_{n\boldsymbol{k}}$) of an electron in band n and with wavevector $\boldsymbol{k}$, as a result of the diffusion and scattering effects, just cancel each other out if the system remains in a steady state, even under a driving electric field. Furthermore, the diffusion term on the right-hand side of the above equation can be approximated by keeping only up to the linear terms of the electric field strength E, which is

$$\left(\frac{\partial f_{n\boldsymbol{k}}}{\partial t}\right)_{\text{diff}} \approx -e\mathscr{E} v_{n\boldsymbol{k}} \partial f^0_{n\boldsymbol{k}}/\epsilon_{n\boldsymbol{k}} \tag{2}$$

where $\mathscr{E}$, $\epsilon_{n\boldsymbol{k}}$, and $v_{n\boldsymbol{k}}$ stand for electric field strength, electron band energy, and velocity component along the electric field orientation, and e is the conventional physical constant. Note that in the right-hand side of the above expression, the electronic stationary distribution function $f_{n\boldsymbol{k}}$ has been approximated with the Fermi-Dirac distribution function $f^0_{n\boldsymbol{k}}$. In terms of the first-order perturbation theory, the collision term arising from the e-ph scattering in Eq. (1) can be derived, and it takes a form as [26,27]

$$\left(\frac{\partial f_{n\boldsymbol{k}}}{\partial t}\right)_{\text{coll}} = \frac{e\mathscr{E}}{k_B T}\sum_{m\boldsymbol{q}} P_{n\boldsymbol{k},m\boldsymbol{k}+\boldsymbol{q}}(F_{n\boldsymbol{k}} - F_{m\boldsymbol{k}+\boldsymbol{q}}) \tag{3}$$

where k_B and T are the Boltzmann constant and temperature, respectively. $F_{n\boldsymbol{k}}$ is the mean-free path, which will be solved from the BTE. The e-ph scattering rate $P_{n\boldsymbol{k},m\boldsymbol{k}+\boldsymbol{q}}$ between the specific electron initial state ($n\boldsymbol{k}$) and final state ($m\boldsymbol{k}+\boldsymbol{q}$) is given by

$$\begin{aligned} P_{n\boldsymbol{k},m\boldsymbol{k}+\boldsymbol{q}} = \frac{2\pi}{\hbar}\sum_{\nu} &\left|g^{\nu}_{mn}(\boldsymbol{k},\boldsymbol{q})\right|^2 f^0_{n\boldsymbol{k}}\left(1 - f^0_{m\boldsymbol{k}+\boldsymbol{q}}\right) \\ &\times [(n_{\boldsymbol{q}}+1)\delta(\epsilon_{n\boldsymbol{k}} - \hbar\omega_{\nu\boldsymbol{q}} - \epsilon_{m\boldsymbol{k}+\boldsymbol{q}}) \\ &+ n_{\boldsymbol{q}}\delta(\epsilon_{n\boldsymbol{k}} + \hbar\omega_{\nu\boldsymbol{q}} - \epsilon_{m\boldsymbol{k}+\boldsymbol{q}})] \end{aligned} \tag{4}$$

where $g^{\nu}_{mn}(\boldsymbol{k},\boldsymbol{q})$ stands for the e-ph interaction matrix element, which involves the electronic initial, final states and the phonon mode indexed by ($n\boldsymbol{k}$), ($m\boldsymbol{k}+\boldsymbol{q}$), and ($\nu\boldsymbol{q}$), respectively. The phonon frequency and boson distribution are represented by $\omega_{\nu\boldsymbol{q}}$ and $n_{\boldsymbol{q}}$. To combine the diffusion and collision term worked out above, the BTE can then be written in an iterative form with the mean-free path as the unknown. It reads [26]

$$F^{i+1}_{n\boldsymbol{k}} = F^0_{n\boldsymbol{k}} + \frac{\tau_{n\boldsymbol{k}}}{f^0_{n\boldsymbol{k}}\left(1 - f^0_{n\boldsymbol{k}}\right)}\sum_{\nu\boldsymbol{q}m} P_{n\boldsymbol{k},m\boldsymbol{k}+\boldsymbol{q}} F^i_{m\boldsymbol{k}+\boldsymbol{q}} \tag{5}$$

where the superscripts of the mean-free path represent the order of the adjacent iteration steps; and $F^0_{n\boldsymbol{k}} = \tau_{n\boldsymbol{k}} v_{n\boldsymbol{k}}$. Note that we have defined the relaxation time of electron in the state $|n\boldsymbol{k}\rangle$ as

$$\tau_{n\boldsymbol{k}} = \left[\sum_{\nu\boldsymbol{q}m} P^{\nu}_{n\boldsymbol{k},m\boldsymbol{k}+\boldsymbol{q}}\right]^{-1}. \tag{6}$$

Of course, the reciprocal of $\tau_{n\boldsymbol{k}}$ stands for the electronic-state resolved scattering rate. For convenience of the discussion of the numerical results of the intrinsic resistivity shown in the next section, we need to further define the energy (E) resolved scattering rate as

$$\tau(E)^{-1} = \sum_{\nu}\tau^{\nu}(E)^{-1} = \sum_{\nu}\frac{\sum_{n\boldsymbol{k}m\boldsymbol{q}} P^{\nu}_{n\boldsymbol{k},m\boldsymbol{k}+\boldsymbol{q}}\delta(E - \epsilon_{n\boldsymbol{k}})}{\sum_{n\boldsymbol{k}}\delta(E - \epsilon_{n\boldsymbol{k}})} \tag{7}$$

in which $\tau^{\nu}(E)^{-1}$ stands for the contributions of individual phonon mode ν to the scattering rate $\tau(E)^{-1}$. Besides, we need also define the average electronic velocity over an isosurface of a given energy E as

$$v(E) = \sqrt{\frac{\sum_{n\boldsymbol{k}} v^2_{n\boldsymbol{k}}\delta(\epsilon_{n\boldsymbol{k}} - E)}{D(E)}} \tag{8}$$

with $D(E) = \sum_{n\boldsymbol{k}}\delta(\epsilon_{n\boldsymbol{k}} - E)$ as the density of states (DOS).

In the form of the BTE given by Eq. (5), the mean-free path can be obtained by performing iteration algorithm. When $F^i_{n\boldsymbol{k}}$'s of adjacent iteration steps converge, the numerically accurate result of the mean-free path is obtained. In contrast, without any iteration procedure we have $F_{n\boldsymbol{k}} \approx F^0_{n\boldsymbol{k}}$, and such a treatment is called the energy relaxation time approximation (ERTA) of the solution of the BTE. Finally, with the obtained mean-free paths, the intrinsic conductivity (σ) and thermal conductivity (κ) can be calculated via the following expressions:

$$\sigma = \frac{e^2}{NSk_BT}\sum_{nk} f^0_{nk}\left(1-f^0_{nk}\right)v_{nk}F_{nk}, \tag{9}$$

$$\kappa = \frac{1}{NSk_BT^2}\sum_{nk} f^0_{nk}\left(1-f^0_{nk}\right)(\epsilon_{nk}-E_f)^2 v_{nk}F_{nk} - \frac{e^2}{T\sigma}\left[\sum_{nk} f^0_{nk}\left(1-f^0_{nk}\right)(\epsilon_{nk}-E_f)v_{nk}F_{nk}\right]^2, \tag{10}$$

where E_f, N, and S are the Fermi energy and the number of unit cells and the area of the unit cell.

III. SIMULATION DETAILS

Using the Quantum ESPRESSO (QE) [28,29] software package along with norm-conserving pseudopotential [30], we performed the first-principles calculations about the electronic band structure and phonon dispersion within the theoretical framework of density functional theory (DFT) [31] and density functional perturbation theory (DFPT) [32]. The generalized gradient approximation (GGA) in the Perdew-Burke-Ernzerhof (PBE) [33] form is used as the exchange-correlation functional. The plane-wave basis is used with a sufficiently high-energy cutoff of 680 eV for better accuracy. Then, a 16 × 16 × 1 Monkhorst Pack grid is used to sample k points in the Brillouin zone (BZ) for the calculation of the electronic structure, while a 8 × 8 × 1 grid of q points is used in the phonon calculations. Such a BZ sampling is far from dense enough for reaching a high-precision calculations on the electronic transport coefficients since only a few k and q points fall in the vicinity of Fermi surface. However, first-principles calculations on a much finer k mesh or q mesh imply a huge computational burden. To circumvent such a prohibitive task, we adopt a generalized Fourier interpolation approach, realized by the EPW code [34] in real space, which allows affordable and accurate calculations of the electronic and phonon energy spectra as well as the e-ph interaction matrix elements on ultrafine k mesh and q mesh.

IV. NUMERICAL RESULT

The lattice structure of goldene is shown in Fig. 1(a). It can be seen that goldene bears an analogy with graphene in that they have the same Bravais lattice and all atoms are strictly positioned in the same planar sheet without undulation. However, unlike graphene, in each unit cell of goldene there is only one Au atom. The optimized lattice constant of goldene is 2.77 Å, which is close to the experimental results (2.62 Å [22]). The phonon dispersion calculated by DFPT is shown in Fig. 1(b). Since gold is a heavy atom, we have also calculated the phonon dispersion after taking into account the spin-orbit coupling (SOC). It can be seen that SOC modifies the phonon dispersion trivially, causing only a slight hardening of the long-wavelength phonons of the out-of-plane vibration mode. What is more, from Fig. 1(b) we observe no imaginary frequencies in the phonon dispersion, regardless of whether the SOC is taken into account. This suggests that goldene maintains a stable 2D lattice structure. Since the unit cell contains only one atom, there are only three acoustic phonon modes and no optical phonons. It can also be seen in this figure that the highest frequency, i.e., the Debye frequency, of these acoustic phonons is also very low, only 180 cm^{-1} (about 259 K).

As for the electronic structure of goldene, the calculated energy bands along high symmetric lines in the BZ and the corresponding DOS spectrum is shown in Fig. 1(c). Firstly, it can be seen from the energy band structure that goldene is a metal, and there is only one energy band passing through the Fermi level. Secondly, the dispersion of the band around the Fermi level is very sharp, which gives a large average Fermi velocity (1.05×10^6 m/s), even larger than the average Fermi velocity of graphene (4.45×10^5 m/s). This result implies that goldene is expected to be a good conductor, comparable to the carrier-doped graphene. The SOC effect is also taken into account in the calculation of the energy bands. Just like the case of the aforementioned phonon dispersion, SOC does not bring about nontrivial modification on the energy bands, especially around the Fermi energy. From the DOS spectrum it can be seen that the DOS around the Fermi energy is very small, in comparison to that of other energy region, consistent with the local strong dispersion of the band around Fermi level, as mentioned above. The energy bands around the Fermi level are mainly contributed by atomic p_x and p_y orbitals (52%), with a certain percentage of s orbitals (22%), degenerated $d_{x^2-y^2}$ and d_{xy} orbitals (26%) as well. This is slightly different compared to the bulk material of gold, where the energy bands near the Fermi surface are mainly contributed by s and p orbitals [35]. As for the band much above the Fermi level, three p orbitals play the dominative role, while the band deep below the Fermi level is mainly composed of d_{xz}, d_{yz}, and d_{z^2}. Given that goldene is a monolayer two-dimensional material, the interatomic bonding is expected to align within the xy plane. Moreover, the primary extension direction of the aforementioned orbitals also lies within the xy plane, thus rendering the aforementioned results comprehensible. Finally, the Fermi surface is shown in Fig. 1(d), and we can see that goldene has a very sizable hexagonal Fermi surface, filling the most part of the BZ.

As the central task of present paper, we now turn to investigate intrinsic resistivity ($\rho = \sigma^{-1}$) of goldene, which, generally speaking, determines the transport characteristic of metallic materials at room temperature. With the formulation presented above, we can perform the first-principles calculation on the ρ-T relation of goldene. The numerical results are shown in Fig. 2(a) where we fix the electric field orientation along the a axis specified in Fig. 1(a). However, since the anisotropy of the intrinsic resistivity is small ($\leqslant$ 5%) according to our numerical results, we will not specifically mention the transport direction hereafter. The weak anisotropy of the intrinsic resistivity is a direct reflection of the Fermi surface geometry without a strong anisotropy. As observed from Fig. 2(a), first of all, ρ-T curves start to show linear profile from an onset temperature even below room temperature. This is a reasonable result since the Debye temperature of goldene is only 259 K. According to our previous study [36], the linear temperature dependence of the intrinsic resistivity of metallic materials usually occurs even from a lower temperature than the Debye temperature. Then, it can be found that the iteration

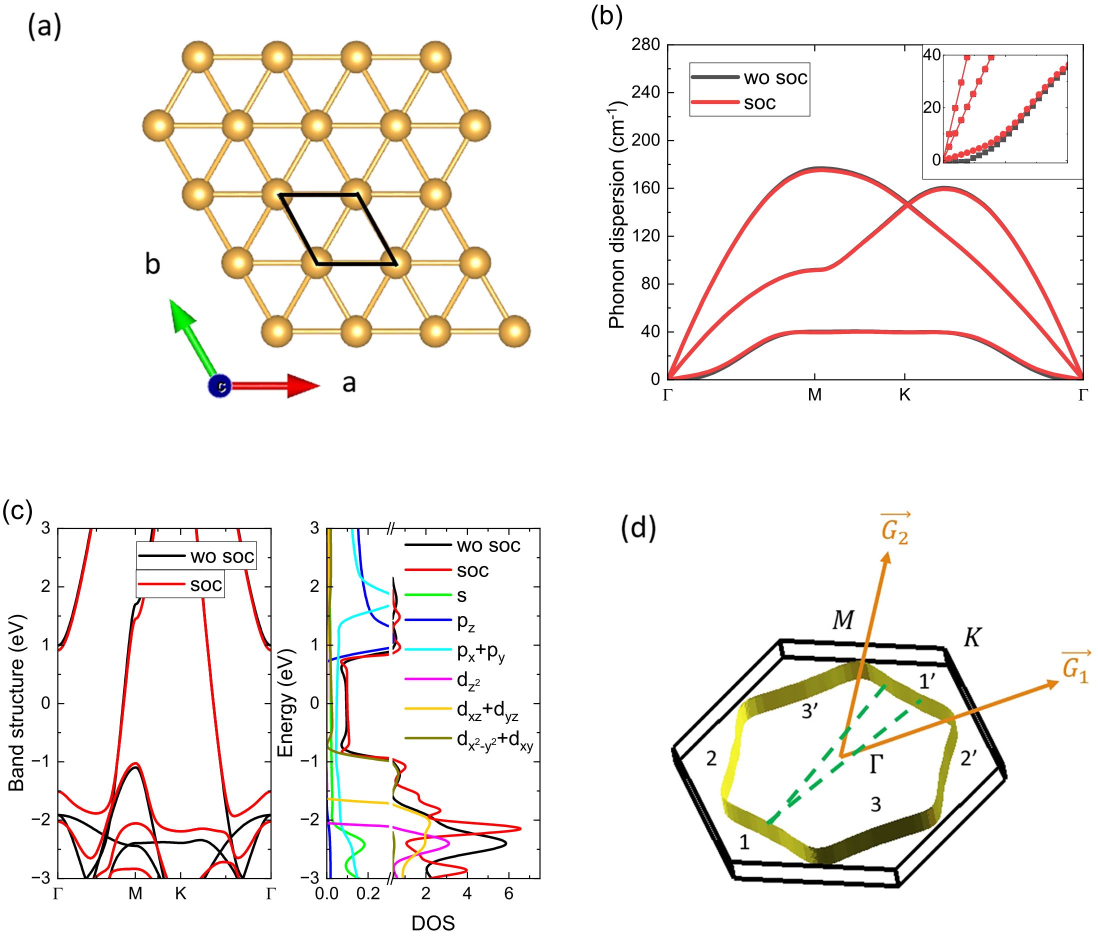

FIG. 1. (a) Top view of the crystal structure of goldene, the unit cell is marked by the black lines. (b) The phonon dispersion without and with spin-orbit coupling (SOC) is plotted as black and red lines respectively. Inset shows the detail of the phonon dispersion in the long-wavelength limiting. (c) The energy bands (left panel) and DOS (right panel). The results without and with SOC are plotted in black and red respectively. The Fermi energy is set as the energy reference point. The DOS spectrum projected to atomic *s*, *p*, and *d* orbitals is also plotted. Since p_x and p_y, d_{xz}, and d_{yz}, and d_{xy} and $d_{x^2-y^2}$ contribute equally to the DOS spectrum, we have drawn them together. (d) The Fermi surface of goldene, plotted in yellow. The black boundary represents the first Brillouin zone. The numbers label the three sets of parallel boundaries of the Fermi surface. The orange arrows denote the reciprocal lattice vectors. Fermi surface nesting effect can be realized by some specific wavevectors connecting the opposite boundaries of the quasihexagonal Fermi surface, shown as an example by the green-dashed lines.

procedure does not bring about a substantive variation on the intrinsic resistivity, although it results in a somewhat quantitative modification of the value of ρ, in comparison with the result of ERTA. As seen from Fig. 2(a), what we would like to emphasize is that at 300 K the intrinsic resistivity of goldene is about 18.6 Ω, from the numerical result of the iteration approach with the SOC effect. It is a very small value, comparable to that of lightly doped graphene (with hole doping concentration of 1.73×10^{10} cm^{-2}), and smaller by one or two orders of magnitude than other 2D metallic materials experimentally accessible such as MXene and plumbene [18,27,37,38]; a detailed comparison can be found in Table I. Besides, by a simple valuation, we find that the conductance of goldene monolayer is equal to that of a gold film with a thickness of about 1 nm. However, it is doubtful whether the thickness of a gold film can be reduced to such a small size even by the state-of-art nanotechnology, with the excellent conductivity of 3D bulk surviving to nanoscale. In contrast, the goldene is so far available. Thus, we can say that goldene is a good 2D conductor with ultrahigh conductivity in a much wider temperature range around the room temperature. In view of its thickness of single atom layer and perfect planar structure, goldene is expected to be a promising material of

TABLE I. The electrical conductivity and thermal conductivity of goldene, hole-doped graphene, borophene, plumbene, Ti_3C_2, Ti_2C, and Ti_2B_2 at room temperature (300 K).

2D material	Conductivity (mS)	Thermal conductivity (nW/K)
Goldene	53.8	237
Doped graphene	119	476
Borophene	38.1 [39]	43.3 [40]
Plumbene	3.26 [27]	0.467–5.33 [41]
Ti_3C_2 (MXenes)	1.63 [42]	33.7 [43]
Ti_2C (MXenes)	11.1 [44]	27.1 [45]
Ti_2B_2 (MBenes)	3.41 [46]	37.5 [47]

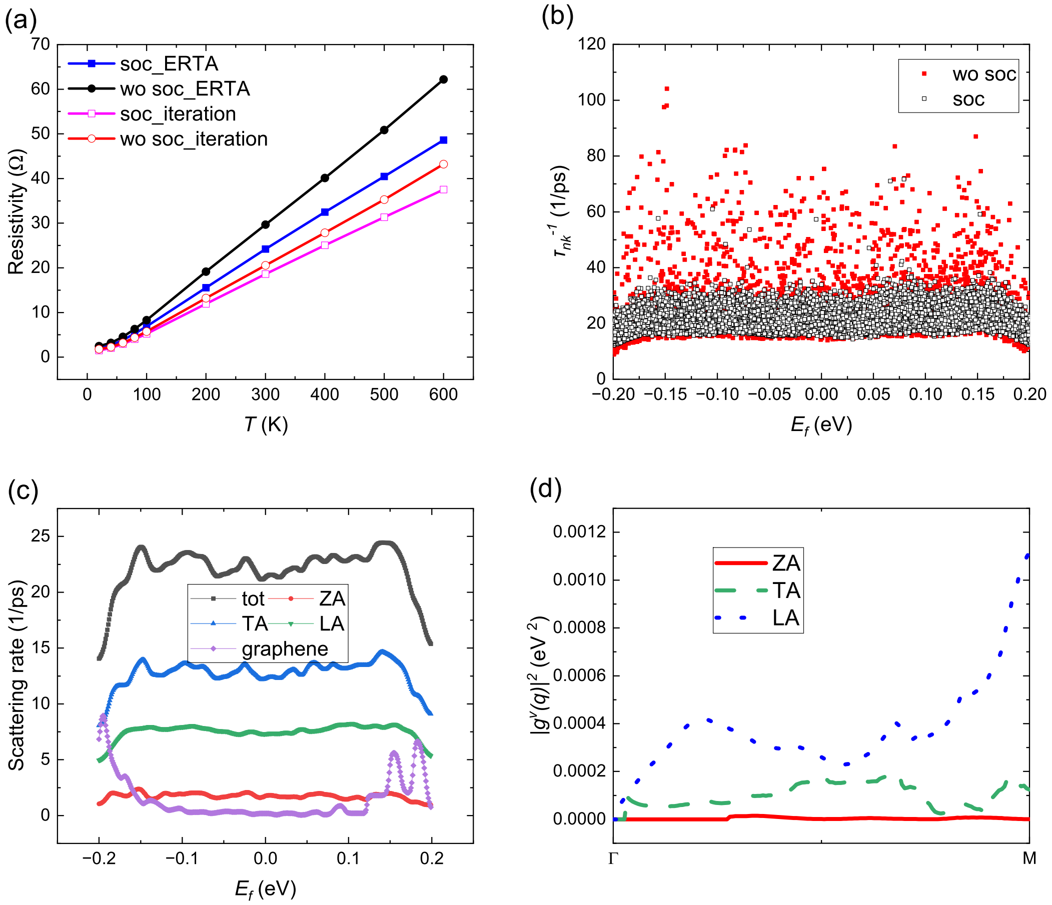

FIG. 2. (a) Intrinsic resistivity of goldene as a function of temperature, where the results obtained by ERTA and iteration method for the two cases with and without SOC are shown in distinct colors, as specified by the legend in the figure. (b) The scattering rates τ_{nk}^{-1} of the electronic states in the Fermi shell, plotted in the order of energy. The results with and without SOC are compared. (c) The energy resolved scattering rates $\tau(E)^{-1}$ and $\tau^\nu(E)^{-1}$ corresponding to the ZA, TA, and LA phonons. These results are plotted in black, red, blue, and green, respectively. For comparison, $\tau(E)^{-1}$ of carrier doped graphene is also plotted in purple, which is much smaller than its counterpart in goldene. (d) The average modular square of e-ph interaction matrix elements over the Fermi shell is plotted as a functions of the phonon wavevector q. As labeled with vertical axis, such a quantity is denoted as $|g^\nu(q)|^2$, which is defined as $|g^\nu(q)|^2 = \langle |g^\nu_{mn}(\boldsymbol{k},\boldsymbol{q})|^2\rangle$ where $\langle\cdots\rangle$ means an averaging over n, m, and $\boldsymbol{k}$ for the electronic states in the Fermi shell. The red, green, and blue curves denote the results of ZA, TA, and LA phonons, respectively.

conductive wires in the electronic devices of next era, instead the 3D bulk gold.

We now go into details about the respective roles of the electronic structure and e-ph scattering on the intrinsic resistivity of goldene. At first, from Fig. 2(a), we can see that SOC cause a slight decrease of the calculated resistivity in the entire temperature range shown. It implies that SOC facilitates the electronic transport, although it is not a very strong effect. In Fig. 2(b), we plot the scattering rates τ_{nk}^{-1} of all the electronic states in the Fermi shell, a relatively thin energy region around Fermi surface of a thickness of 0.4 eV. It is easy to understand that in the temperature range considered in Fig. 2(a) only the electronic state in such a Fermi shell is active for the electronic transport. We can see from Fig. 2(b) that in comparison with the case without SOC, the high scattering rates of some electronic states are effectively suppressed, which perhaps arises from the quantum interference between the electronic probability amplitudes of two opposite spin components introduced by SOC. Besides, our numerical calculation indicates that the average velocity $v(E)$ in the Fermi shell is also slightly enhanced by SOC, although it is so small that the difference of the band dispersion around Fermi level between the two cases with and without SOC is indistinguishable on the scale as shown in Fig. 1(c). It is obvious that such an enhancement of $v(E)$ by SOC favors the electronic transport. These two factors, i.e., the suppression of large $1/\tau_{nk}$ of some electronic states and the slight enhancement of $v(E)$, combine to be responsible for the mild decrease of resistivity by SOC observed in Fig. 2(a).

In Fig. 2(c) we plot the numerical results of the phonon mode resolved scattering rates $\tau^\nu(E)^{-1}$ versus E in the Fermi shell, which indicates that the TA and LA phonons have larger scattering rate than the ZA phonon. This is due to the decoupling of the flexural phonon, i.e., the ZA phonon in the long-wavelength limit, from e-ph interaction, which also occurs in other 2D materials such as graphene with mirror symmetry normal to the material plane. Such a situation is demonstrated by the numerical result shown in Fig. 2(d) where the average modular square of the e-ph interaction matrix element between electron in Fermi shell and phonons in different modes as a function of q along a high symmetry line $(\Gamma - M)$ is plotted. As expected, the e-ph interaction matrix element of the ZA phonon is much smaller than that of the LA and TA phonons. This is why the ZA phonon contributes a very small scattering rate despite being the most easily excited phonon mode. Herein, to digress for a moment, let us make a few remarks on the effect of ripples in actual sample as a kind of disorder on the electronic transport in goldene. The ondulations of the actual structure of any goldene sample are inevitable, which had been observed in the original study of synthesizing the goldene sample [22]. The structural ondulation, also called ripples, is ubiquitous in many 2D material of single-atomic-layer thickness, e.g., goldene and graphene [48], As a kind of disorder, ondulations will impact necessarily the electronic transport property in goldene to some extent. If the ondulation is weak enough to be viewed as a perturbation, just following the decoupling mechanism of flexural phonon from e-ph scattering process as discussed in the context of our paper, such a disorder is expected to be free from scattering electrons in transport process in goldene, thanks to the mirror symmetry. However, when the ondulation has large amplitude in the normal direction of the sample sheet and its leading wavelength reduces to nanoscale, it can no longer be viewed as a perturbation (the mirror symmetry is broken). It modifies the electronic states, the phonon spectrum and the e-ph interaction nontrivially. As a result, it will influence the conductivity of goldene in a very complicated way. So far it remains a formidable task to study the effect of the structural ondulation on the intrinsic resistivity of 2D materials on the level of first-principles calculations. This is beyond the scope of the present paper. Now let us come back to discuss the results presented in Fig. 2; from Fig. 2(c) we can also find that the total scattering rate $\tau(E)^{-1} = \sum_{\nu} \tau^{\nu}(E)^{-1}$ of goldene is much larger than that of doped graphene. This is because that the Au atom is much heavier than C atom. Consequently, the phonon dispersion in goldene is overall much lower than that in graphene, which is thus easier to be excited to take part in e-ph scattering. The strong e-ph scattering justifies why the intrinsic resistivity of goldene around room temperature is still larger than that of the lightly doped graphene, although the latter has smaller Fermi velocity and DOS at Fermi surface.

It is well known that the large-angle e-ph scattering plays the leading role in limiting the intrinsic resistivity of a metal or semiconductor. Goldene has a very large Fermi surface, which implies that the large-angle e-ph scattering to determine the intrinsic resistivity is realized by phonons with relatively large q. In addition, because of the hexagonal geometry of the Fermi surface as shown in Fig. 1(d), Fermi surface nesting is expected to be the important mechanism to determine the intrinsic resistivity. In Fig. 3(a), the typical sets of $\boldsymbol{q}$'s for realizing Fermi surface nesting are labeled. It is obvious that those nesting vectors $\boldsymbol{q}$'s connecting the opposite boundaries of the Fermi surface realize the large-angle scattering. Therefore, they correspond to the phonons (TA and LA), which have the leading contribution to the resistivity. In Fig. 3(b) we plot the calculated nesting function, i.e., $\xi(\boldsymbol{q}) = \sum_{nmk} \delta(\epsilon_{nk} - E_f)\delta(\epsilon_{mk+q} - E_f)$, which demonstrates unambiguously the importance of the nesting vectors $\boldsymbol{q}$'s plotted together with the Fermi surface in Fig. 3(a).

We now pay attention to the electronic thermal conductivity of goldene. In view of its high conductivity revealed above, goldene is highly likely to be an excellent thermal conductor if it obeys the empirical Wiedemann-Franz law, which says that $\kappa/(\sigma T) = L_0$. As a good approximation for a lager number of metals, the so-called Lorenz constant has a standard value $L_0 = \frac{\pi^2}{3}\frac{k_b^2}{e^2} = 2.44 \times 10^{-8}$ WΩK, which is only determined by physical constant, regardless of the detail of materials. With the use of Eq. (10), we calculate the thermal conductivity of goldene as a function of temperature. The numerical result is shown in Fig. 3(c). It can be seen that at room temperature $\kappa = 237$ nW/K, which is lower than the thermal conductivity of the doped graphene (476 nW/K). But it is still an excellent value of thermal conductivity, in comparison with other 2D materials. The thermal conductivities of typical 2D materials are presented in Table I for comparison with our result of goldene. Notice that we have not taken into account the phonon thermal conductivity since the thermal conductivity of goldene as a good metal is mainly determined by the electronic contribution, and a recent theoretical study reported that the phonon thermal conductivity is much smaller than our above numerical result [49]. Moreover, from Fig. 3(c) it can be seen that the thermal conductivity as a function of T presents a peak on the low-temperature side (about 50 K), then followed by a slow-varying region (100 K $\sim$ 400 K) and finally decreases rapidly in the high-temperature side (>400 K). This result can be briefly explained as follows: In the low-temperature region, with the increase of temperature, the occupation number of the electron states with relatively high energy is enhanced, which favors the thermal transport. However, the e-ph scattering also increases with temperature since more phonons are excited, which goes against the electronic thermal transport. As a result, the thermal conductivity shows a peak at 50 K. The interplay of these two opposite factors brings about the slow-varying behavior of κ in the intermediate temperature shown in Fig. 3(c). When temperature increases further, the e-ph scattering becomes the main mechanism to affect the electronic thermal transport, hence κ goes down rapidly in the high-temperature side as seen in Fig. 3(c). In addition, from this figure it can be found the calculated ratio $\kappa/(\sigma T)$ is always smaller than the standard Lorenz constant in the whole temperature range with the maximal deviation amounting to 25%. However, at 300 K such a deviation is smallest. Thus, goldene conforms to Wiedemann-Franz law satisfactorily at room temperature. From Fig. 1(c) we can see that no nontrivial variation of the energy band dispersion occurs around Fermi level in a large energy range. This suggests that the Fermi surface maintains nearly the same geometry and size even as the Fermi level shifts within this energy range. Consequently, the conductivity and thermal conductivity of goldene are expected to be insensitive to the carrier doping by which the Fermi level is shifted. We calculate σ and κ as functions of Fermi energy level variation relative to its intrinsic value of the charge neutrality, which is shown in Fig. 4(b). It can be seen that both of σ and κ show a flat region within the range $-0.60 \sim 0.40$ eV of the Fermi level variation. This energy range corresponds to a range of the carrier doping concentration from -5.59×10^{13} cm^{-2} (hole) to 5.80×10^{13} cm^{-2} (electron). This is another feature of

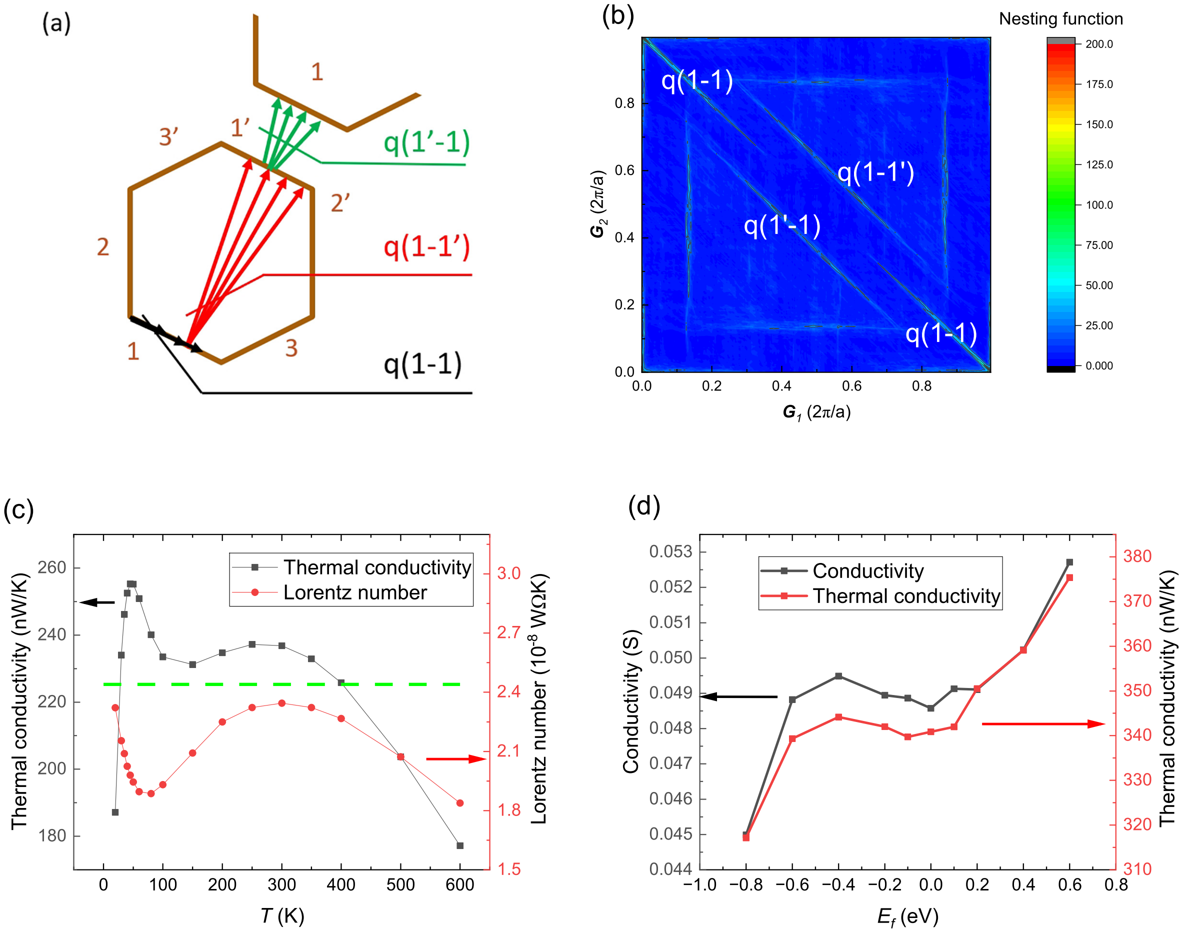

FIG. 3. (a) The intact and partial hexagons mimic the Fermi surface of goldene as shown in Fig. 1(d) duplicated in the adjacent BZs. Three sets of nesting wavevectors associated with the two opposite boundaries 1 and 1′ of the Fermi surface are labeled by arrows and denoted by $\boldsymbol{q}(1-1')$, $\boldsymbol{q}(1'-1)$, and $\boldsymbol{q}(1-1)$, respectively. Note that the similar nesting wavevectors associated with the other boundaries of the hexagonal Fermi surface are not shown for brevity. (b) Plot of the nesting function vs $\boldsymbol{q}$, where the horizontal and vertical axes gives the projections of wavevector $\boldsymbol{q}$ along the reciprocal lattice vectors $\boldsymbol{G}_1$ and $\boldsymbol{G}_2$ as labeled in Fig. 1(d). Some highlighted lines just correspond to the nesting wavevectors shown in (a). The remaining highlighted lines correspond to the nesting wavevectors associated with other boundaries of the Fermi surface. (c) Thermal conductivity and Lorenz number vs temperature. The green-dashed line indicates the standard value of Lorenz number, i.e., $L_0 = 2.44 \times 10^{-8}$ WΩK. (d) Conductivity and thermal conductivity as a function of the variation of the Fermi level relative to its intrinsic value of the charge neutrality.

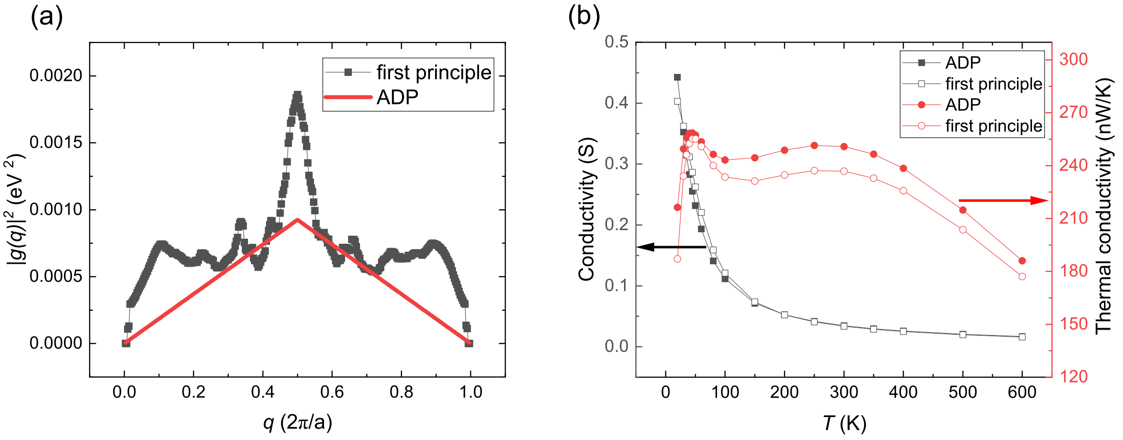

FIG. 4. (a) The average modular square of the e-ph interaction matrix elements (black square) as a function of q. With a given q the averaging is performed over the electronic states in the Fermi shell. As a result of numerical fitting, the modular square (red line) of the e-ph interaction matrix elements of the ADP model is also shown for comparison. (b) The numerical results of conductivity and thermal conductivity vs temperature obtained by ADP and the first-principles calculations for comparison.

the transport properties of goldene as a good 2D conductor, besides the high electric and thermal conductivity.

For semiconductors and metals with small Fermi surface, the relevant phonons to determine the intrinsic resistivity is limited in the long-wavelength region. In such a situation, one can often employ a simple theoretical model to describe the e-ph scattering, called the acoustic deformational potential (ADP) model. And usually, such a model can give semiquantitative evaluation of the intrinsic resistivity of materials. In this model the modular square of the complex e-ph interaction matrix elements is approximated by a simple form as $|g^{\nu}_{mn}(\boldsymbol{k},\boldsymbol{q})|^2 \approx |g(q)|^2 = \Xi^2|q|$, where Ξ is an empirical parameter, i.e., the so-called ADP parameter. For the case of goldene, as mentioned above, the intrinsic resistivity is not limited by the long-wavelength phonons. In such a case, we wonder whether an appropriate ADP model can be established to describe the e-ph scattering limited transport properties satisfactorily. By numerical calculations we find such a ADP model is available if the ADP parameter takes a proper value. We obtain such a parameter value by calculating $\langle|g^{\nu}_{mn}(\boldsymbol{k},\boldsymbol{q})|^2\rangle$ as a function of q where $\langle\cdots\rangle$ means an averaging over the phonon modes ν's and electronic wavevector $\boldsymbol{k}$ and band indices of electronic states in the Fermi shell. Then, by a simple fitting $\langle|g^{\nu}_{mn}(\boldsymbol{k},\boldsymbol{q})|^2\rangle \approx |g(q)|^2 = \Xi^2|q|$, we can get the proper value of $\Xi = 11.6\ \text{meV}\sqrt{\text{Å}}$. $\langle|g^{\nu}_{mn}(\boldsymbol{k},\boldsymbol{q})|^2\rangle$ and $|g(q)|^2 = \Xi^2|q|$ as a function of $\boldsymbol{q}$ along a high symmetric line in the BZ is plotted in Fig. 4(a). Note that in our ADP model a cutoff value of q is required, specifically $q_c = \pi/a$. When $q > q_c$ we use $q = q - q_c$. In Fig. 4(b), we compare the σ-T and κ-T curves obtained by the first-principles calculations and the ADP model. We can see that simple ADP model works very well in calculating these transport coefficients of goldene.

V. CONCLUSIONS

In the present paper, by means of the first-principles calculations, we perform a systematic study on the electronic structure, phonon dispersion, and electronic transport properties limited by e-ph scattering of goldene, a planar single atomic layer of gold successfully fabricated much recently. First of all, we find that goldene hosts only three acoustic phonon modes owing to its crystal nature of a monatomic Bravais lattice. The Debye frequency (259 K) is much lower than many typical 2D materials such as graphene due to the relatively heavy mass of gold atom. Goldene is a 2D metal, and the electronic structure around Fermi level is simple. There is only one band spanning the Fermi level. But it is notable that in goldene the electron around Fermi level is featured by a very large Fermi velocity, more than double of that in graphene. This electron feature is in favor of the outstanding electronic transport properties of such a 2D gold material. Then, by calculating the intrinsic conductivity limited by e-ph scattering, we find goldene does possess an ultrahigh conductivity in a wide temperature range around 300 K, which ranks only second to the carrier doped graphene, and much higher than other typical 2D metallic materials such as MXenes and MBenes. According to these a numerical results, we estimate that goldene, as an atomically thin 2D metal, has the conductance equivalent to that of a 1-nm-thick gold film, assuming that the excellent electronic transport properties of 3D gold bulk are remained at the nanoscale. In more details, we find that the intrinsic resistivity of goldene shows a linear temperature dependence even below 300 K. Such a low temperature onset for the linear ρ-T relation is closely related to the fact that goldene has a low Debye frequency. The LA and TA phonons play the leading role on determining the intrinsic resistivity of goldene. In contrast, the ZA mode corresponding the out-of-plane atomic vibration almost completely decouples from the e-ph scattering due to the mirror symmetry. Finally, we establish a simple deformational potential model to describe the e-ph interaction, which works very well to reproduce the numerical result of first-principles calculation of the intrinsic conductivity of goldene. Therefore, this model is very useful for quickly interpreting experimental results on the electronic transport properties of goldene samples. In short, our theoretical findings indicate that the recently created goldene presents ultrahigh intrinsic electrical and thermal conductivity. Therefore, it is expected to be a promising material for conductive wires in the next-generation electronic devices, instead of the 3D bulk gold.

ACKNOWLEDGMENTS

This work was financially supported by the National Natural Science Foundation of China (Grants No. 12174145 and No. 11774123) and the Fundamental Research Funds for the Central Universities. We thank the High Performance Computing Center of Jilin University for their calculation resource.

---

[1] L.-Y. Zhu, L.-X. Ou, L.-W. Mao, X.-Y. Wu, Y.-P. Liu, and H.-L. Lu, Advances in noble metal-decorated metal oxide nanomaterials for chemiresistive gas sensors: Overview, Nano-Micro Lett. **15**, 89 (2023).

[2] Y. Chen, Q. Qiao, J. Cao, H. Li, and Z. Bian, Precious metal recovery, Joule **5**, 3097 (2021).

[3] Y. Yan, T. Wang, X. Li, H. Pang, and H. Xue, Noble metal-based materials in high-performance supercapacitors, Inorg. Chem. Front. **4**, 33 (2017).

[4] Y. Nafde and R. Pande, Design, and analysis of resistive series RF MEMS switches based fractal U-slot reconfigurable antenna, Wireless Personal Commun. **97**, 2871 (2017).

[5] Kurmendra and R. Kumar, A review on RF micro-electro-mechanical-systems (MEMS) switch for radio frequency applications, Microsystem Technologies **27**, 2525 (2021).

[6] Z. Zhao, D. Deng, B. Bachmatiuk, S. Sandeep, P. Popov, J. Eckert, and M. H. Rümmeli, Free-standing single-atom-thick iron membranes suspended in graphene pores, Science **343**, 1228 (2014).

[7] X. Wang, C. Wang, C. Chen, H. Duan, and K. Du, Free-standing monatomic thick two-dimensional gold, Nano Lett. **19**, 4560 (2019).

[8] F. Yang, S. Cheng, X. Zhang, X. Ren, R. Li, H. Dong, and W. Hu, 2D organic materials for optoelectronic applications, Adv. Mater. **30**, 1702415 (2018).

[9] Q. Qiu and Z. Huang, Photodetectors of 2D materials from ultraviolet to terahertz waves, Adv. Mater. **33**, 2008126 (2021).

[10] D. Akinwande, C. J. Brennan, J. S. Bunch, P. Egberts, J. R. Felts, H. Gao, R. Huang, J.-S. Kim, T. Li, Y. Li *et al.*, A review on mechanics, and mechanical properties of 2D materials-graphene, and beyond, Ext. Mech. Lett. **13**, 42 (2017).

[11] S. Das, A. Sebastian, E. Pop, C. J. McClellan, A. D. Franklin, T. Grasser, T. Knobloch, Y. Illarionov, A. V. Penumatcha, J. Appenzeller *et al.*, Transistors based on two-dimensional materials for future integrated circuits, Nat. Electron. **4**, 786 (2021).

[12] X. Liu, M. S. Choi, E. Hwang, Won J. Yoo, and J. Sun, Fermi level pinning dependent 2D semiconductor devices: Challenges, and prospects, Adv. Mater. **34**, 2108425 (2022).

[13] C. Dai, Y. Liu, and D. Wei, Two-dimensional field-effect transistor sensors: The road toward commercialization, Chem. Rev. **122**, 10319 (2022).

[14] Y. Liu, S. Zhang, J. He, Z. M. Wang, and Z. Liu, Recent progress in the fabrication, properties, and devices of heterostructures based on 2D materials, Nano-Micro Lett. **11**, 13 (2019).

[15] E. Elahi, G. Dastgeer, P. R. Sharma, S. Nisar, M. Suleman, M. W. Iqbal, M. Imran, M. Aslam, and A. Imran, A brief review on the spin valve magnetic tunnel junction composed of 2D materials, J. Phys. D: Appl. Phys. **55**, 423001 (2022).

[16] E. C. Ahn, 2D materials for spintronic devices, npj 2D Mater. Appl. **4**, 17 (2020).

[17] A. Cultrera, D. Serazio, A. Zurutuza, A. Centeno, O. Txoperena, D. Etayo, A. Cordon, A. Redo-Sanchez, I. Arnedo, M. Ortolano, and L. Callegaro, Mapping the conductivity of graphene with electrical resistance tomography, Sci. Rep. **9**, 10655 (2019).

[18] L. Jia, S. Zhou, A. Ahmed, Z. Yang, S. Liu, H. Wang, F. Li, M. Zhang, Y. Zhang, and L. Sun, Tuning MXene electrical conductivity towards multifunctionality, Chem. Eng. J. **475**, 146361 (2023).

[19] X. Xu, Y. Zhang, H. Sun, J. Zhou, F. Yang, H. Li, H. Chen, Y. Chen, Z. Liu, Z. Qiu, D. Wang, L. Ma, J. Wang, Q. Zeng, and Z. Peng, Progress, and perspective: MXene, and MXene-based nanomaterials for high-performance energy storage devices, Adv. Electron. Mater. **7**, 2000967 (2021).

[20] Z. Guo, J. Zhou, and Z. Sun, New two-dimensional transition metal borides for Li ion batteries, and electrocatalysis, J. Mater. Chem. A **5**, 23530 (2017).

[21] R. Li, Y. Wang, L.-C. Xu, J. Shen, W. Zhao, Z. Yang, R. Liu, J.-L. Shao, C. Guo, and X. Li, A boron-exposed $\mathrm{TiB_3}$ monolayer with a lower electrostatic-potential surface as a higher-performance anode material for Li-ion, and Na-ion batteries, Phys. Chem. Chem. Phys. **22**, 22236 (2020).

[22] S. Kashiwaya, Y. Shi, J. Lu, D. G. Sangiovanni, G. Greczynski, M. Magnuson, M. Andersson, J. Rosen, and L. Hultman, Synthesis of goldene comprising single-atom layer gold, Nat. Synth. **3**, 744 (2024).

[23] J. Bardeen and W. Shockley, Deformation potentials, and mobilities in non-polar crystals, Phys. Rev. **80**, 72 (1950).

[24] J. M. Ziman, *Electrons, and Phonons: The Theory of Transport Phenomena in Solids* (Oxford University Press, Oxford, 2001).

[25] J. M. Ziman, *Principles of the Theory of Solids*, 2nd ed. (Cambridge University Press, Cambridge, 1972).

[26] W. Li, Electrical transport limited by electron-phonon coupling from Boltzmann transport equation: An *ab initio* study of Si, Al, and $\mathrm{MoS_2}$, Phys. Rev. B **92**, 075405 (2015).

[27] S. Zhao, M. Zhu, and Y. Zheng, Modified Ziman resistivity formula valid for the case of the Fermi level near a band edge, J. Phys. Chem. C **127**, 13978 (2023).

[28] P. Giannozzi, S. Baroni, N. Bonini, M. Calandra, R. Car, C. Cavazzoni, D. Ceresoli, G. L Chiarotti, M. Cococcioni, I. Dabo *et al.*, Quantum Espresso: A modular, and open-source software project for quantum simulations of materials, J. Phys.: Condens. Matter **21**, 395502 (2009).

[29] P. Giannozzi, O. Andreussi, T. Brumme, O. Bunau, M. B. Nardelli, M. Calandra, R. Car, C. Cavazzoni, D. Ceresoli, M. Cococcioni *et al.*, Advanced capabilities for materials modelling with quantum espresso, J. Phys.: Condens. Matter **29**, 465901 (2017).

[30] J. P. Perdew and Y. Wang, Accurate, and simple analytic representation of the electron-gas correlation energy, Phys. Rev. B **45**, 13244 (1992).

[31] W. Kohn and L. J. Sham, Self-consistent equations including exchange, and correlation effects, Phys. Rev. **140**, A1133 (1965).

[32] S. Baroni, S. de Gironcoli, A. Dal Corso, and P. Giannozzi, Phonons, and related crystal properties from density-functional perturbation theory, Rev. Mod. Phys. **73**, 515 (2001).

[33] J. P. Perdew, K. Burke, and M. Ernzerhof, Generalized gradient approximation made simple, Phys. Rev. Lett. **77**, 3865 (1996).

[34] S. Poncé, E. R. Margine, C. Verdi, and F. Giustino, Epw: Electron-phonon coupling, transport, and superconducting properties using maximally localized Wannier functions, Comput. Phys. Commun. **209**, 116 (2016).

[35] T. Rangel, D. Kecik, P. E. Trevisanutto, G.-M. Rignanese, H. Van Swygenhoven, and V. Olevano, Band structure of gold from many-body perturbation theory, Phys. Rev. B **86**, 125125 (2012).

[36] Z. Liu, M. Zhu, and Y. Zheng, Fermi surface nesting, and intrinsic resistivity of beryllium: First-principles calculations, Phys. Rev. B **100**, 045145 (2019).

[37] B. Anasori, M. R. Lukatskaya, and Y. Gogotsi, 2D metal carbides, and nitrides (MXenes) for energy storage, Nat. Rev. Mater. **2**, 16098 (2017).

[38] J. L. Hart, K. Hantanasirisakul, A. C. Lang, B. Anasori, D. Pinto, Y. Pivak, J. T. van Omme, S. J. May, Y. Gogotsi, and M. L. Taheri, Control of MXenes' electronic properties through termination, and intercalation, Nat. Commun. **10**, 522 (2019).

[39] Z. Liu, M. Zhu, and Y. Zheng, First-principles calculations on the intrinsic resistivity of borophene: Anisotropy, and temperature dependence, J. Mater. Chem. C **7**, 986 (2019).

[40] H. Sun, Q. Li, and X. G. Wan, First-principles study of thermal properties of borophene, Phys. Chem. Chem. Phys. **18**, 14927 (2016).

[41] D. K. Das and B. Kumar, Variation of heat flow rate of vertically arranged plumbene sheets with number of layers, and sample size, Mod. Phys. Lett. B **38**, 2450033 (2024).

[42] A. D. Dillon, M. J. Ghidiu, A. L. Krick, J. Griggs, S. J. May, Y. Gogotsi, M. W. Barsoum, and A. T. Fafarman, Highly

conductive optical quality solution-processed films of 2D titanium carbide, Adv. Funct. Mater. **26**, 4162 (2016).

[43] M. Wang, Y. Liu, H. Zhang, Y. Wu, and L. Pan, Thermal conductivities of $Ti_3C_2T_x$ mxenes, and their interfacial thermal performance in MXene/epoxy composites—A molecular dynamics simulation, Int. J. Heat Mass Transf. **194**, 123027 (2022).

[44] Z. Jing, J. Liu, N. Li, H. Wang, K. Wu, Y. Cheng, and B. Xiao, Electron-phonon scattering limited intrinsic electrical conductivity of metallic MXenes X_2C ($X = $ Ti or Mo), J. Phys. D: Appl. Phys. **54**, 015301 (2021).

[45] S. Sarikurt, D. Çakır, M. Keçeli, and C. Sevik, The influence of surface functionalization on thermal transport, and thermoelectric properties of MXene monolayers, Nanoscale **10**, 8859 (2018).

[46] H. Zhang, M. Zhu, and Y. Zheng, First principles study on the intrinsic resistivity of rectangular Ti_2B_2, and Mo_2B_2, Phys. Rev. B **108**, 245425 (2023).

[47] D. Li, Y. Hu, G. Ding, C. Feng, and D. Li, Remarkable decrease in lattice thermal conductivity of transition metals borides TiB_2 by dimensional reduction, Nanotechnology **33**, 235706 (2022).

[48] I. N. Kholmanov, C. W. Magnuson, A. E. Aliev, H. Li, B. Zhang, J. W. Suk, L. L. Zhang, E. Peng, S. H. Mousavi, A. B. Khanikaev, R. Piner *et al.*, Improved electrical conductivity of graphene films integrated with metal nanowires, Nano Lett. **12**, 5679 (2012).

[49] B. Mortazavi, Goldene: An anisotropic metallic monolayer with remarkable stability, and rigidity, and low lattice thermal conductivity, Materials **17**, 2653 (2024).